Disentangling UV photodesorption and photoconversion rates of H2O ice at 20 K: measured with laser desorption post ionization mass spectrometry

Bulak, M.; Paardekooper, D.M.; Fedoseev, G.; Samarth, P.; Linnartz, H.V.J.

Astronomy & Astrophysics

Disentangling UV photodesorption and photoconversion rates of H_2O ice at 20 K

Measured with laser desorption post ionization mass spectrometry

M. Bulak[1], D. M. Paardekooper[1], G. Fedoseev[1,2], P. Samarth[1], and H. Linnartz[1]

[1] Laboratory for Astrophysics, Leiden Observatory, Leiden University, PO Box 9513, 2300 RA Leiden, The Netherlands
e-mail: bulak@strw.leidenuniv.nl
[2] Research Laboratory for Astrochemistry, Ural Federal University, Kuibysheva St. 48, 620026 Ekaterinburg, Russia

ABSTRACT

Context. The nondissociative ultraviolet photodesorption of water ice is a nonthermal desorption mechanism required to account for detected abundances of gas-phase water toward cold regions within the interstellar medium. Previous experimental and theoretical studies provide a range of photodesorption rates for H_2O ice and point to a convoluted competition with other molecular processes following the absorption of a UV photon in the ice. Ultraviolet irradiation also induces photodissociation, resulting in the formation of radicals that may directly desorb triggering gas-phase reactions or recombine in surface reactions.

Aims. In this work, we aim to quantify the effects of photodesorption and investigate photoconversion upon UV photolysis of an H_2O ice.

Methods. We irradiated a porous amorphous H_2O ice at 20 K with UV photons in the 7–10.2 eV range and compared the measurements to a nearly identical experiment that included a layer of argon coating on top of the water ice. The purpose of the argon coating is to quench any type of photon-triggered desorption. To trace ice composition and thickness, laser desorption post ionization time-of-flight mass spectrometry was utilized. This method is independent of the (non)dissociative character of a process and provides a diagnostic tool different from earlier studies that allows an independent check.

Results. The total photodesorption rate for a porous amorphous H_2O ice at 20 K we derive is $(1.0 \pm 0.2) \times 10^{-3}$ per incident UV photon (7–10.2 eV), which is in agreement with the available literature. This rate is based on the elemental balance of oxygen-bearing species. As a result, we placed an upper limit on the intact (H_2O) and dissociative (OH) desorption rates equal to 1.0×10^{-3} per incident UV photon, while for the reactive desorption (O_2), this limit is equal to 0.5×10^{-3} per incident UV photon. Photoconversion depletes the H_2O ice at a rate of $(2.3 \pm 0.2) \times 10^{-3}$ per incident UV photon. At low UV fluence (9.0×10^{17} photons cm^{-2}), the loss of H_2O is balanced by photoproduct formation (O_2 and H_2O_2). At high UV fluence (4.5×10^{18} photons cm^{-2}), about 50% of the initial H_2O molecules are depleted. This amount is not matched by the registered O-bearing products, which points to an additional, unaccounted loss channel of H_2O.

Key words. astrochemistry – molecular processes – methods: laboratory: solid state – protoplanetary disks – ISM: molecules – ultraviolet: ISM

1. Introduction

Water (H_2O) is ubiquitous in the interstellar medium (ISM) and plays a key role in the physics and chemistry of the star- and planet-forming regions. It is the most abundant constituent of the interstellar ice mantles (Gibb et al. 2004; Boogert et al. 2008) and has an observed gas-phase trail in different environments, including in diffuse and translucent clouds (Flagey et al. 2013), prestellar cores (Caselli et al. 2012), star-forming regions (Ceccarelli et al. 2010), protoplanetary disks (Hogerheijde et al. 2011), and comets (Hartogh et al. 2011). The observed abundances of water in the ice and gas are intricately linked and provide information on local physical conditions.

The majority of water in the ISM resides in interstellar ices with an average abundance of solid H_2O with respect to gas-phase H_2 equal to 1.0×10^{-4} (e.g., Pontoppidan et al. 2004; Boogert et al. 2015; Whittet et al. 2013). Water ice is mainly formed on cold dust grains (10–20 K) via surface hydrogenation reactions with O, OH, O_2, and O_3

(Tielens & Hagen 1982; Bergin et al. 2000; Ioppolo et al. 2008, 2010; Miyauchi et al. 2008; Lamberts et al. 2013). An additional low-temperature formation channel is available via gas-phase chemistry. This contribution is limited by the efficiency of the involved ion-molecule reaction scheme and is capable of reproducing the water abundances of H_2O/H_2 at the level of $(0.5–1.5) \times 10^{-8}$ only, equivalent to abundances found in translucent clouds (Bergin et al. 1995; Jensen et al. 2000; Hollenbach et al. 2009). An alternative gas-phase formation pathway via neutral-neutral chemistry becomes efficient only above temperatures of 250 K (Harada et al. 2010).

Ice chemistry is coupled with processes in the gas phase via accretion and desorption processes. In regions with temperatures between 10 and 20 K, observed gas-phase water abundances cannot be accounted for by gas-phase formation or thermal desorption; hence, nonthermal desorption mechanisms need to be considered (Willacy & Langer 2000; Boonman et al. 2003; Öberg et al. 2009b; Hollenbach et al. 2009; Walsh et al. 2010; Oka et al. 2012). This has been the case for observations toward

photon dominated regions of molecular clouds (Snell et al. 2000; Wilson et al. 2003), prestellar cores (Caselli et al. 2012), outer parts of protostellar envelopes (Schmalzl et al. 2014), and proto-planetary disks (Dominik et al. 2005; Willacy 2007; Hogerheijde et al. 2011). The nonthermal desorption mechanism that is used to explain these observations is UV photodesorption of water ice. This mechanism, initiated by a UV photon absorption, allows species in the ice to be transferred into the gas phase. For this process to take place, UV photons are required, which originate from the interstellar radiation field (ISRF) and nearby proto-stars. In regions where ISRF is attenuated by dust grains (i.e., cores of dense clouds or protoplanetary disks), the (lower) pho-ton flux originates from interactions of cosmic rays with H_2, resulting in a secondary UV field, with emission peaking at Ly-α (Prasad & Tarafdar 1983; Gredel et al. 1989). For these reasons, photodesorption of interstellar ice analogues has been studied in detail, both experimentally and theoretically, for a num-ber of different molecules, including CO, CO_2, CH_4, CH_3OH, and H_2O.

An experimental determination of the photodesorption rate is inherently challenging due to the convoluted competition between photodesorption and photoconversion in UV-irradiated interstellar ices (see Fig. 1 in Bulak et al. 2020). Photoconver-sion is characterized by a combination of the following two solid state processes: photodissociation, followed by recombination reactions into photoproducts (defined as photochemistry), and reactions of nondissociated, photoexcited molecules, with neigh-boring neutral species. Both types of reactions provide the formation pathways of many of the simple and complex species observed in the ISM (e.g., Gerakines et al. 1996; Garrod et al. 2008; Öberg et al. 2009a; Paardekooper et al. 2016a; Bulak et al. 2021). Competition between photodesorption and photoconver-sion usually takes place for species with a bond dissociation energy below the energy of impacting UV photons, which applies to most constituents of interstellar ices found in the dense molecular clouds, H_2O, CO_2, CH_4, NH_3, CH_3OH. The com-mon exceptions are CO and N_2, which have a bond dissociation energy above 10.2 eV.

The photodesorption and photoconversion of H_2O ice have been extensively studied experimentally (Westley et al. 1995; Gerakines et al. 1996; Öberg et al. 2009b; DeSimone et al. 2013; Cruz-Diaz et al. 2018) and with molecular dynamics simulations (Andersson et al. 2006; Andersson & van Dishoeck 2008; Arasa et al. 2010, 2011, 2015; Koning et al. 2013). In the original lab-oratory studies by Westley et al. (1995), a quartz microbalance was used to monitor the depletion of H_2O ice upon UV irradia-tion and used to derive the photodesorption rate. Simultaneously, photodesorbed gas-phase species (H_2 and O_2) were monitored by quadruple mass spectrometry (QMS). In a study focusing on the photoconversion of H_2O ice, Gerakines et al. (1996) used infrared spectroscopy to detect the formation of HO_2, H_2O_2, and OH in ice. In the work by Öberg et al. (2009b), the photode-pletion upon UV radiation (7–10.2 eV) of the H_2O and D_2O ices was monitored using reflection-absorption infrared spec-troscopy (RAIRS), while the gas-phase species were probed by QMS. Based on the collected RAIRS data, the photodesorption rate of H_2O ice was derived. Mass spectrometry measurements allowed for detection of the photodesorption of OH, a gas-phase product of solid water photodissociation, as well as other photo-products (H_2, O_2). In more recent studies (Cruz-Diaz et al. 2018; Fillion et al. 2022), a QMS was used to measure the gas-phase signal during photolysis of H_2O (D_2O) ice. Based on the calibra-tion of the QMS, the signal was converted to a photodesorption rate of H_2O, OH, and O_2. In the work of Fillion et al. (2022), a wavelength selective (and not a broadband) approach was used, as originally introduced for CO ice by Fayolle et al. (2011).

The aforementioned diagnostic tools (i.e. IR spectroscopy and QMS) have been proven to be capable tools for quantifying the photon-triggered processes, providing a range of photodes-orption rates for H_2O ice at different low temperatures between $(1–4) \times 10^{-3}$ molecule photon^{-1}. However, a method also capable of distinguishing the effect of photodesorption and pho-toconversion in water ice is still missing. Infrared spectroscopy allows the tracing of photodepletion in the parent species, which is a combined effect of both processes (i.e., photodesorption and photoconversion). It is a method that requires molecules to have an IR-active transition, which means that nonpolar species, such as one of the photoproducts, O_2, are not directly detectable. In addition, there is an uncertainty associated with the interpreta-tion of the IR data linked to a possible overlap of vibrational features of the parent species (H_2O) with photoproducts (OH) and the mathematical deconvolution of the photodesorption rate. Quadruple mass spectrometry offers a solution to these issues with a direct measurement of photodesorbed species; however, it also comes with limitations: QMS measures an equilibrated gas-phase composition in the chamber, which means that molecules, prior to being detected, may interact with the walls and other inner parts of the setup. The conversion of the gas-phase signals to a photodesorption rate is also challenging (Fayolle et al. 2011; Martín-Doménech et al. 2015; Bertin et al. 2016). Additionally, with a QMS-only approach, the effect of photoconversion in the ice remains unconstrained.

In this study of UV photolysis of amorphous water ice, we apply a different but complimentary experimental approach that was previously used to measure the photodesorption of CO (Paardekooper et al. 2016b) and was shown to separate pho-todesorption effects from photoconversion in pure ices of CH_4, CH_3OH, and CH_3CN (Bulak et al. 2020). Laser desorption post ionization time-of-flight mass spectrometry (LDPI TOF MS) was used to probe the ice composition and thickness as a func-tion of UV fluence. To determine the effect of each process, pure H_2O ice photolysis experiments were compared to measurements from similar experiments that additionally included an argon coating. The purpose of the argon layer was to quench any type of photon-triggered desorption with a minimal effect on the photo-conversion. The comparison of coated and uncoated experiments was used to trace the photoconversion and photodesorption pro-cesses, and to quantify the latter. The next section includes a summary of the experimental procedure, while the results, dis-cussion, and astrophysical implications are described in Sects. 3, 4, and 5, respectively.

2. Experimental setup

A detailed description of the used setup MATRI^{2}CES (Mass Analysis Tool to study Reactions in Interstellar ICES) has been provided in Paardekooper et al. (2014). The experimental pro-cedure that we used is described in Bulak et al. (2020). In this section, we only briefly discuss the relevant details.

2.1. Experimental system

The MATRI^{2}CES setup consists of a main and time-of-flight mass spectrometer (TOF MS) chamber with a base pressure in the ~10^{-10} mbar range. In the main chamber, ices are deposited onto a chemically inert gold surface cooled with a closed-cycle helium cryostat to 20 K. The cryostat is mounted on a two-dimensional translation stage that allows for the

manipulation of the substrate position along the horizontal and vertical axes. The temperature of the substrate is regulated in the 20–300 K range (relative precision of ±0.25 K) using a thermocouple and a resistive heater in thermal contact with the substrate, controlled by a Lakeshore temperature controller. Prior to deposition, liquid water samples of $H_2^{16}O$ (miliQ) or $H_2^{18}O$ (Sigma-Aldrich, 97%^{18}O) are purified from air contamination via three freeze-pump-thaw cycles. Argon gas (≥99 999% purity, Linde) is used without further purification. The deposition of (H_2O and Ar) vapors proceeds nearly orthogonal through a capillary pointed at 85 degrees with respect to the substrate plane. The ice growth rate is controlled via a calibrated high-precision needle valve. As a result of deposition at 20 K, we formed a thin film of porous amorphous solid water (ASW) with an ice column density of 20×10^{15} molecules cm^{-2} (20 monolayers, MLs; assuming 1 ML = 1×10^{15} molecules cm^{-2}). Prior laser interference measurements were used to estimate the deposition rate by measuring the absolute thickness of the H_2O ice (see Bulak et al. 2020 for details). The uniformity of the ice thickness across the substrate was expected within ±1.5 ML. The thickness of the deposited argon coating was 50 ML, sufficient to prevent any forms of photodesorption in the underlaying ice (see Bulak et al. 2020).

The photolysis was performed with a microwave discharge hydrogen lamp (MDHL), which emits UV photons in the range between 121.6 and 170 nm. This corresponds to an energy range of 7.2–10.2 eV. The spectral energy distribution of the lamp is given in Ligterink et al. (2015; see Fig. 4 therein), and the UV photon flux was calibrated at the location of the substrate using a Si diode to be $(2.5 \pm 0.5) \times 10^{14}$ photons cm^{-2} s^{-1}.

Laser desorption post ionization time-of-flight mass spectrometry was used to quantitatively probe the composition of the ice. An unfocused laser shot (Nd:YAG, Polaris II, 4-5 ns) trimmed to a beam diameter of approximately 1.5 mm and with a typical pulse energy of about 55 mJ per cm^2 was guided onto the deposited ice at an incident angle of 30 degrees with respect to the plane perpendicular to the substrate. This pulse, optimized to trigger a complete local desorption, transferred the species from the ice phase into the gas phase. The resulting plume was subsequently ionized via a continuous electron impact ionization source with a mean electron energy of 70 eV. As the ionized plume traveled through the ion optics, a part of it was extracted with a short voltage pulse (typical duration of 4 μs) that guided the charged species into the field-free TOF MS (operated in reflectron mode). During the drift, ions were separated based on their mass-to-charge ratio (m/z). Their time-of-flight, from the ion extraction area to the Z-gap micro channel plate detector (MCP), was recorded with a data acquisition card (DAQ) at a sampling rate of 2.5×10^8 Hz. This probing technique was synchronized between the trigger of the laser at 5 Hz with an automated translation of the substrate along the vertical direction, which allowed the probing of 100 fresh locations on the substrate (along the z-axis). The LDPI TOF MS of these 100 fresh spots along a single column was then averaged to provide a single LDPI TOF MS with a high signal-to-noise ratio. To track changes in the ice as a function of UV photon fluence, the substrate was then translated along the horizontal direction, and the probing scheme was repeated to provide another LDPI TOF MS composed of 100 averages along the new vertical column. This was then repeated for each UV dose until the substrate could no longer be horizontally translated. The TOF traces were collected and averaged using a Labview routine.

The probing sequence of the laser shot, the ion extraction pulse, and the data acquisition were controlled with a delay
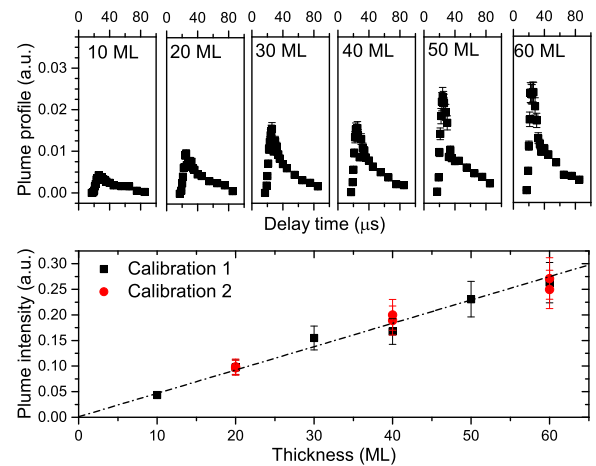
Fig. 1. Calibration measurements for LDPI TOF MS of H_2O ice. Top panel: LDPI TOF MS plume profiles for different initial H_2O ice thickness at 20 K. The intensity is the sum of the m/z = 17 (OH$^+$) and m/z = 18 (H_2O^+) signals, which are the two major fragment masses upon electron impact ionization of water. Profiles were collected as a function of the delay time between laser desorption and ion extraction. Bottom panel: total signal of the integrated plume profiles from the top panel as a function of initial ice thickness of amorphous H_2O ice, collected during two independent calibration measurements. The data were fitted with a linear function (R^2 = 0.98).

generator (DG 535, Stanford Research System). A variation in a relative time delay between the laser shot and the ion extraction pulse (between 17 and 80 μs) allowed us to sample the complete profile of the plume. The collected TOF traces were subsequently converted to mass spectra, with a mass resolution of $\Delta m/m \sim 250$.

All experiments and resulting conclusions in this work are based on the elemental balance of oxygen-bearing species; that is, we look exclusively at the impact the UV light has on the H_2O abundance with and without irradiation by measuring the gas-phase abundance of oxygen-bearing species without and with an Ar cap, respectively. The LDPI TOF MS signature of H_2O ice used here therefore consists of mass peaks at m/z = 16, 17, and 18, which are fragments formed upon the electron impact ionization event: O$^+$, OH$^+$, and H_2O^+, accordingly (Kim et al. 2014). Due to the low relative intensity of the mass peak at m/z = 16 (1% of m/z = 18), only peaks at m/z = 17 and 18 were used for analysis. For control experiments with $H_2^{18}O$, peaks at m/z = 19, and 20 were used.

We focused on the oxygen balance to derive the H_2O photodesorption rate, as it is not necessary to take into account photodesorbing H or H_2. In fact, for these species – which barely stick to a surface when below 20 K – no experimental photodesorption rates exist, mainly because of the challenges involved. The most important one is that at UHV conditions, the residual amount of H_2 gas in the chamber is substantially higher than what would be released from the ice surface, complicating such measurements.

The sum of the calculated intensities of the H_2O features in the plume profile was proportional to the thickness of the ice (Paardekooper et al. 2014; Bulak et al. 2020). To demonstrate this, H_2O ices of different initial thickness (10–60 ML) were deposited and analyzed with LDPI TOF MS. In Fig. 1, the total intensity of the recorded plume profile is shown as a function of the deposited ice thickness. The plot includes data from two separate calibration experiments that probe ices with different initial

ice thickness. The demonstrated linear relationship allowed us to use the integrated plume profile obtained with LDPI TOF MS as a direct measurement of the ice thickness.

2.2. Experimental overview

The experimental approach enabled us to determine the photodesorption yield by subtracting the phoconversion yield from the total photodepletion yield. Following the approach of Bulak et al. (2020), the first type of experiment probed the photodepletion of pure H_2O ice. The measured loss of H_2O is linked to the photodissociation (photoexcitation) of the parent species followed by formation of photoproducts (photoconversion) as well as photodesorption of the water molecules, its fragments, and the photoproducts. The second type of experiment was performed with an additional layer of argon (50 ML) deposited on top of the H_2O ice. The purpose of the coating was to quench photodesorption processes, including intact, dissociative, and reactive photodesorption (being surface or subsurface processes). Argon, as a noble gas, does not interact with the photodissociation products of H_2O. In addition, the argon coating is transparent in the UV range (Schnepp & Dressler 1960), allowing for direct comparison of the two experiments. The difference in the photodepletion of H_2O between uncoated and coated experiments was used to derive a total photodesorption rate in the H_2O ice.

A challenge associated with measuring the photodesorption of water ice is to exclude the contribution from the residual gas-phase water present in the vacuum chamber, even at ultra high vacuum (UHV) conditions. The H_2O freeze-out is most efficient immediately after the ice deposition, and it continues during the UV photolysis (see Westley et al. 1995; Öberg et al. 2009b), which was also the case in our system. The issue was circumvented by considering the relative difference in the photodepletion rate between the coated and uncoated experiments, both of which include the contribution from the residual gas freeze-out. Hence, contamination was present; however, its impact on the derived photodesorption rate is limited. The same reasoning was applied to the uncertainty related to other experimental parameters: UV photon flux and ice thickness calibration. Under the assumption that the argon layer has a minimum effect on the photon flux reaching the H_2O ice, these main sources of uncertainty (photon flux and ice thickness) cancel each other out during the derivation of the photodesorption yield. Hence, the error margin in this work is based on the reproducibility of the repeated measurements (15% for both coated and uncoated experiments), which leads to a final uncertainty of 21% on the photodesorption yield. This value is relatively high but not larger than the uncertainty reported in photodesorption experiments using RAIRS and/or TPD QMS techniques.

The experimental parameters were constrained in the following way. The initial ice thickness was set within the characterized linear range (see Fig. 1) that is above the threshold (4–5 ML) at which photodesorption is no longer expected to be a zeroth order process (Öberg et al. 2009b; Muñoz Caro et al. 2010; Fayolle et al. 2011; Chen et al. 2014). The substrate temperature during the deposition and irradiation was kept at 20 K, the minimum reachable temperature with MATRI²CES and which represents the warmer regions of dense molecular clouds. To be able to monitor the photodepletion of H_2O abundance as a function of photon fluence, the ices were exposed, incrementally, to a total UV photon fluence of 4.5×10^{18} photons cm^{-2}. The experiments with the argon coating were performed at the same temperature,

which is well below the sublimation threshold of argon (between 30 and 40 K).

3. Results

Figure 2A shows the LDPI TOF MS spectra of H_2O ice at 20 K prior to the UV irradiation. The recorded plume profile, based on the characteristics of the peaks for water (OH^+ and H_2O^+), was used as a reference spectrum to track changes in the ice as a function of UV photon fluence. The data presented in the figure monitor the full plume, which was recorded at different extraction times between 17 and 71 μs; for this reason, ions OH^+ and H_2O^+ were recorded several times (see Sect. 2.1). To demonstrate the evolution of the H_2O ice upon UV irradiation, Fig. 2B shows the LDPI TOF MS plume profile recorded after a UV dose of 2.7×10^{18} photons cm^{-2}. The plume (without argon coating) shows the same distribution profile, with a clear decrease in the intensity of the ion signals, which is linked to the photodepletion of the H_2O ice.

To derive the photodepletion rate, the LDPI TOF MS plume profiles were recorded at six increments of UV photon fluence, with the final fluence equal to 4.5×10^{18} photons cm^{-2}. Figure 2C shows the corresponding integrated LDPI TOF MS spectra, which were converted to the ice column density following the methods described in Sect. 2. The resulting column density as a function of UV fluence (for experiments with both $H_2^{16}O$ and $H_2^{18}O$) are plotted in Fig. 2D. The best fit to the data is provided by a linear function ($R^2 = 0.989$) where the slope represents the photodepletion rate of H_2O ice at 20 K. The calculated value is equal to $(3.4 \pm 0.1) \times 10^{-3}$ molecule photon^{-1}. It accounts for losses of amorphous H_2O ice due to photoconversion and photodesorption events. After the maximum photon fluence of 4.5×10^{18} photons cm^{-2}, 75% of the H_2O ice was depleted, yielding a final column density of $(5.1 \pm 1.5) \times 10^{15}$ molecules cm^{-2}.

A similar analysis was performed on the LDPI TOF MS spectra of H_2O ice capped with an argon layer (50 ML) at 20 K, shown in Fig. 3(A–D). In the mass spectra prior to UV irradiation, in addition to the features assigned as originating from H_2O, a signal representing Ar^+ is traced (Fig. 3A, upper plot). To investigate the decrease of the coated H_2O ice upon UV irradiation, the plume profile after a fluence of 3.6×10^{18} photons cm^{-2} is shown for both H_2O products and Ar (Fig. 3B). The integrated mass peaks for all UV fluence increments were then converted into the corresponding ice column densities (Figs. 3C and D). The data from the $H_2^{16}O$ and $H_2^{18}O$ experiments was fitted with a linear function with a slope equal to $(2.3 \pm 0.3) \times 10^{-3}$ molecule photon^{-1} ($R^2 = 0.99$). In the experiment with argon coating, the loss of H_2O via photodesorption channels was quenched, while the loss channel due to photoconversion remained active. After the maximum photon fluence of 4.5×10^{18} photons cm^{-2}, ~55% of the H_2O ice was depleted, resulting in a column density of $(9.2 \pm 1.5) \times 10^{15}$ molecules cm^{-2}. Due to the timing optimized for H_2O, we were not able to trace the complete argon plume. This, however, has no effect on the derived H_2O photodepletion.

The final step of analysis was examining the difference between the depletion rate of the coated and uncoated experiments and linking it to the total photodesorption efficiency of the ice. Figure 4 shows the comparison of the results from the coated and uncoated experiments. The difference between them was fitted with a linear function with a slope of the
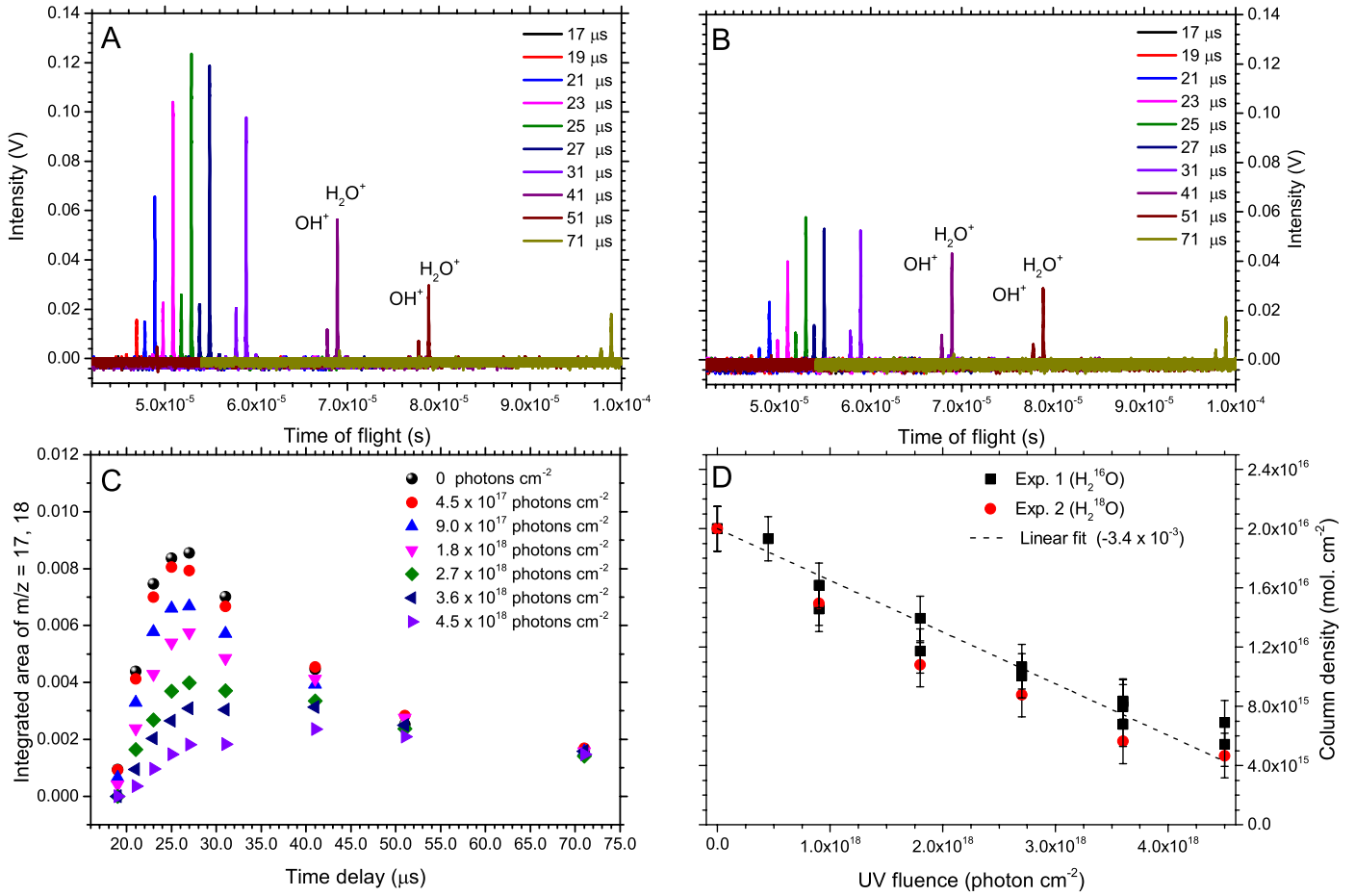
Fig. 2. LDPI TOF MS spectra of H_2O ice at 20 K prior and during the UV irradiation, followed by their quantitative analysis. Panel A: LDPI TOF MS spectra of porous amorphous H_2O ice (20 ML) collected at 20 K, prior to UV photolysis. Panel B: LDPI TOF MS spectra of porous amorphous H_2O ice after UV irradiation with a photon fluence of 2.7×10^{18} photons cm^{-2}. In the plots shown in panels A and B, the labeling of the ions is representative for each full plume; however, for clarity of the figure, we kept the labeling minimal. Panel C: integrated plume profiles of LDPI TOF MS signals for different UV photon fluence increments. Panel D: photodepletion of the H_2O column density as a function of UV fluence from repeated experiments with $H_2^{16}O$ and $H_2^{18}O$. Error bars represent the uncertainty regarding the ice thickness of ± 1.5 ML.

fit corresponding to the photodesorption rate of $(1.0 \pm 0.2) \times 10^{-3}$ molecule photon^{-1}. This value represents the total photodesorption efficiency of porous amorphous H_2O ice at 20 K.

4. Discussion

4.1. Types of photodesorption

The derived photodesorption rate of amorphous water ice at 20 K is a combination of intact desorption (as H_2O), dissociative desorption (H, OH, or O), and reactive desorption (H_2, O_2). We are only capable of measuring the total photodesorption efficiency, but with this approach we can provide upper limits for the individual contributions listed above. These values are compared with the outcome of previous studies. An overview of all ASW photodesorption rates reported in the literature is provided in Table 1. We note that not all experimental settings (temperature, ice thickness, UV spectral energy distribution, level of porosity/compactness) in these studies are identical, and for this reason, comparisons should be performed with care.

Intact desorption efficiencies measured experimentally for UV photon energies between 7 and 10.2 eV at 8 and 20 K are in the range of $(0.55$–$1.3) \times 10^{-3}$ molecule photon^{-1} (Öberg et al.

2009b; Cruz-Diaz et al. 2018; Fillion et al. 2022). Molecular dynamics studies, which consider photon absorption only into the first excited state of water (8.2–9.5 eV), yield lower values between $(0.14$ and $0.5) \times 10^{-3}$ molecule photon^{-1} (Kobayashi 1983; Andersson & van Dishoeck 2008; Arasa et al. 2010; Crouse et al. 2015). Based on these theoretical investigations, several mechanisms have been proposed that lead to the intact photodesorption of H_2O. An exothermic surface recombination of photodissociation products, OH and H, can result in the H_2O molecule leaving the ice surface. Alternatively, in a "kick-out" mechanism, an H atom transfers its kinetic energy (following dissociation) to a surface molecule, resulting in the ejection of the latter. DeSimone et al. (2013) suggested a third mechanism in which excitons generated in ice upon absorption of UV photons are near the surface where the charge redistribution of the surface water molecules results in a repulsive electrostatic force and is followed by a desorption of an H_2O molecule (Nishi et al. 1984). This mechanism may contribute to the efficiency of total photodesorption rate of water through photodesorption of intact water, in addition to the dissociative mechanism discussed by Andersson et al. (2006).

The contribution of dissociative desorption (OH) varies across different studies. Öberg et al. (2009b) derived a value for the OH desorption as roughly equal to the efficiency
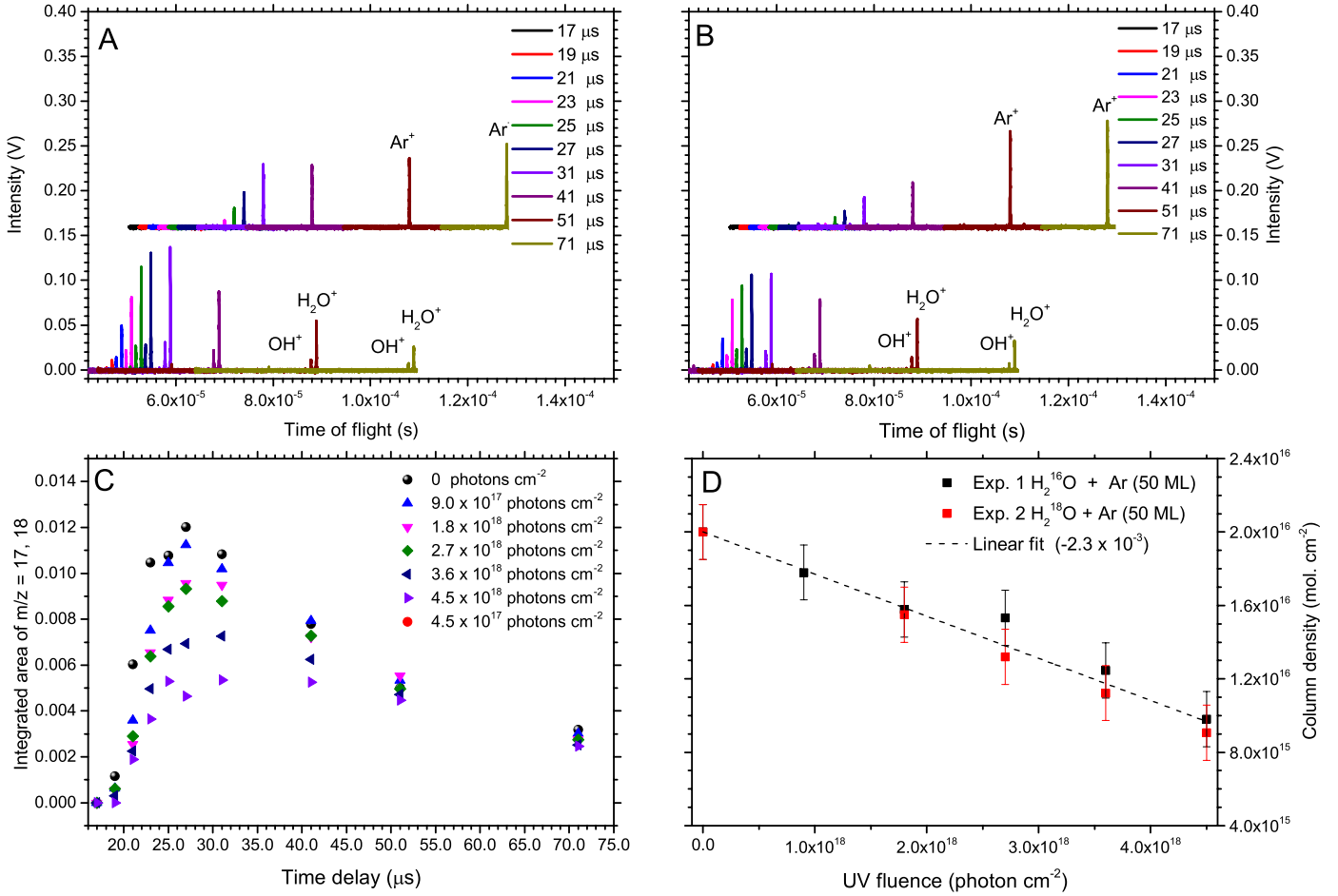
Fig. 3. LDPI TOF MS spectra of H_2O+Ar ice at 20 K prior and during the UV irradiation, followed by their quantitative analysis. Panel A: LDPI TOF MS spectra of porous amorphous $H_2^{16}O$ ice (20 ML) coated with an argon layer (50 ML) and collected at 20 K prior to UV photolysis. For clarity of the figure, the plume profile of Ar^+ is separated and vertically offset. Panel B: LDPI TOF MS spectra of porous amorphous H_2O + Ar ice after a UV irradiation with a fluence of 3.6×10^{18} photons cm^{-2}. In plots shown in panels A and B, labeling of ions is representative for each full plume; however, for clarity of the figure, we kept the labeling minimal. Panel C: integrated plume profiles of LDPI TOF MS for different UV photon fluence increments. Panel D: photodepletion of the H_2O column density as a function of UV fluence from repeated experiments with $H_2^{16}O$ and $H_2^{18}O$. Error bars represent the uncertainty regarding the ice thickness of ±1.5 ML.

of intact water desorption at low temperatures (0.9×10^{-3} molecule photon^{-1}). Cruz-Diaz et al. (2018) provided a yield of 0.7×10^{-3} molecule per incident photon at 8 K, which is lower than their intact photodesorption by a factor of two. In a study by Fillion et al. (2022), OH desorption at 20 K was found to be below their detection limit ($\sim10^{-4}$ molecule photon^{-1}). We find it important to note that with the applied experimental methods (IR and QMS), it is difficult to quantify the contribution of OH from photolysis. In the ice, the OH signature overlaps with a vibrational band of H_2O, while in the gas phase, the corresponding mass peak ($m/z = 17$) can be created as a byproduct of electron impact ionization, rather than UV photolysis. The theoretical studies (Arasa et al. 2010; Crouse et al. 2015) result in rates that are higher than intact desorption, with the ratios of desorbing OH/H_2O between one and two. The absolute calculated desorption yield of OH is lower than the previously reported experimental values, by a factor of two to three (3×10^{-4} molecule photon^{-1}).

Reactive photodesorption from water ice is a mechanism previously detected for photoproducts of H_2 and O_2. The O_2 reactive photodesorption rate was first reported by Öberg et al. (2009b) at a high temperature (100 K), and it was first quantified by

Cruz-Diaz et al. (2018), who determined the reactive photodesorption rate of O_2 at 8 K of $(0.6 \pm 0.3) \times 10^{-3}$ per incident photon. In the study by Fillion et al. (2022), the reactive photodesorption rate of O_2 at 15 K was found to be $(0.3 \pm 0.2) \times 10^{-3}$ per incident photon. We note that the reactive desorption of other photoproducts, such as HO_2 and H_2O_2, is yet to be confirmed. While these are not expected to be major desorption channels, we estimated a conservative upper limit for both species equal to 5.0×10^{-4} per incident photon. Theoretical studies were not able to trace O_2 (or other species) formation and/or desorption due to the short timescales of the modeled processes.

To summarize, the literature provides a range of values for total UV photodesorption of water, between (0.37 and 3.5) $\times 10^{-3}$ per incident photon. These values span an order of magnitude, and there is a systematic difference between theoretical and experimental studies. The results of the most recent experimental studies, including this work, agree within a factor of three with each other. This level of agreement is quite acceptable, given the involved uncertainties and differences in ice temperature, used UV photon sources, and probing techniques. Photodesorption is a wavelength-dependent process (e.g., Fayolle et al. 2011); hence

Table 1. Summary of water ice photodesorption rate studies, both experimental ("Exp.") and theoretical ("Theory"), compared with our work.

Reference	Exp./Theory	H_2O	OH	O_2	Total[1]	Temp. (K)	Energy (eV)
This work	Exp.	<1.0	<1.0	<0.5	1.0 ± 0.2	20	7–10.2
Westley et al. (1995)	Exp.	<3.5	–	–	3.5 ± 1.8	35	10.2
Öberg et al. (2009a)	Exp.	0.7 ± 0.4	0.9 ± 0.5	–	1.6 ± 0.9	10	7–10.2
Cruz-Diaz et al. (2018)	Exp.	1.3 ± 0.2	0.7 ± 0.3	0.6 ± 0.1	3.2 ± 0.5	8	7–10.2
Fillion et al. (2022)[2]	Exp.	0.55 ± 0.09	<0.1	0.3 ± 0.2	1.25 ± 0.25	15	7–10.2
Andersson & van Dishoeck (2008)	Theor.	0.14	0.25	–	0.39	10	8.5
Arasa et al. (2010)	Theor.	0.15	0.3	–	0.55	10	8.5
Crouse et al. (2015)	Theor.	0.3 ± 0.2	0.3 ± 0.2	–	0.6 ± 0.3	11	8.5

Notes. All desorption rates are given in $\times 10^{-3}$ molecule photon^{-1}. The derived rate upper limits are marked by the "<" notation in front of the value. These limits were obtained by consequently considering desorption of the three dominating oxygen species: intact H_2O, OH, and O_2. [1]This value represents the loss of water through intact, dissociative, and reactive photodesorption. As production and desorption of one O_2 molecule requires the consumption of two H_2O molecules, the total photodesorption rate of H_2O was obtained through the sum of the photodesorption rate of intact I suggest using words instead of math symbols (i.e., plus/times). H_2O + OH + 2× O_2. [2]The values listed here are derived from values integrated over the wavelength values covered by the used H_2 microwave discharge lamp (see Paardekooper et al. 2016b).
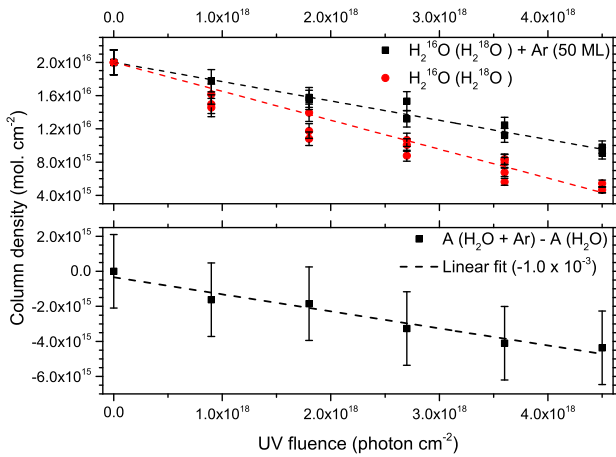
Fig. 4. LDPI TOF MS spectra of H_2O ice at 20 K prior and during the UV irradiation, followed by their quantitative analysis. Top panel: abundance of H_2O during the UV photolysis of H_2O with and without an argon coating at 20 K. Error bars represent the uncertainty regarding the ice thickness of ± 1.5 ML. Bottom panel: the difference in the H_2O abundance between the H_2O and H_2O + Ar experiments resulting in an H_2O photodesorption rate. Error bars represent the propagated uncertainty regarding the ice thickness, with a final value equal to ± 2.1 ML. The data were fitted with a linear function ($R^2 = 0.94$).

the different spectral energy distributions of the applied UV sources can be a reason for differences in measured photodesorption rates. The temperature of the ice during the deposition and irradiation processes is another parameter that impacts the efficiency of photodesorption. A relative increase in the total photodesorption rate for ices irradiated at temperatures between 8 and 30 K was experimentally measured and found to yield values differing by 15% (Cruz-Diaz et al. 2018) to up to 40% (Öberg et al. 2009b). A theoretical study by Arasa et al. (2010) is in agreement with these measurements, as they derived a relative increase in the total photodesorption rate between 10 and 30 K to be 15%. Furthermore, we note that all derived photodesorption rates come with relatively high uncertainties. In the case of experiments, a combination of errors related to ice column density, UV photon flux, (IR) band strength, or varying pumping efficiencies for different species can add up to a large error margin on the final photodesorption rates, which can be as

high as 50%. In theoretical calculations, a difference of a factor of a few mutliples can be caused by the use of the gas-phase potential energy surface for modeling the interactions between H_2O molecules, a short time scale, and only exciting the water molecules into the first excited state (Arasa et al. 2010).

The technique used in this work is based on a diagnostic tool that is different from previous works, and it therefore provides an independent approach to determine the UV photodesorption rate of ASW at 20 K. The LDPI TOF approach that we used provides an alternative way to derive an upper limit for an experimentally derived total photodesorption rate of ASW based on the detection of oxygen-bearing species. The resulting value is well within the uncertainty of other experimental studies and is a factor of two above theoretical results. It provides a basis to constrain each type of photodesorption (i.e., intact, dissociative, and reactive) with an upper limit for the first two types equal to the total derived photodesorption rate, 1.0×10^{-3} molecule photon^{-1}. For the reactive desorption of molecular oxygen, the upper limit is at 0.5×10^{-3} molecule photon^{-1}, whereas for each desorbed O_2, a loss of two H_2O molecules is required. These upper limits are based on the assumption that the total photodesorption is dominated by a contribution from only one channel, while the others are set to zero.

4.2. Photoconversion of H_2O ice

In Fig. 4, the effects of photodesorption and photoconversion during the UV photolysis of H_2O ice can be distinguished from each other. We find it noteworthy that in the coated experiments where the depletion due to photodesorption is excluded, the remaining column density of H_2O is only about 50% of the initial value after the final UV fluence dose. Clearly, upon extended UV irradiation, the ice is subject to more processing than only photodesorption.

Photoconversion is a dominant loss channel, depleting the H_2O molecules at a rate of $(2.3 \pm 0.3) \times 10^{-3}$ per UV photon. We expected the depletion of the parent species to be due to the formation of photoproducts, H_2, OH, O_2, HO_2, and H_2O_2. Only recently, the first quantitative study of the formation of typically elusive O_2 and H_2O_2 was reported – it also applied LDPI TOF MS (Bulak et al. 2022). In experiments favoring bulk processes, the authors of the study exposed an H_2O ice (100 ML thickness) deposited at 20 K to a UV photon fluence of

1.8×10^{18} photons cm^{-2}. The formation of both O_2 and H_2O_2 was found to reach a balance with the available destruction pathways, at roughly equal abundances of 1% (~1 ML) with respect to H_2O, after a UV fluence between $(4.5-9.0) \times 10^{17}$ photons cm^{-2}. Both O_2 and H_2O_2 required two oxygen atoms to be formed (i.e., two H_2O molecules). As these were the only detected products, the corresponding depletion of the parent species was estimated to be 4%. If we assume the same efficiency of photoproduct formation in the experiments with argon coating presented in this work, when exposed to the same irradiation dose, the consumption of water due to photoconversion should be 0.8 ML. This reasoning allows us to account for the loss of H_2O via photoconversion into O_2 and H_2O_2, at least at the early stages, which from an astronomical point of view are the most relevant photolysis stages, but not for the later stages.

At higher photon fluence, the depletion of H_2O continues at a linear rate, while the abundances of detected photoproducts are expected to either remain on the same level or decrease (Bulak et al. 2022). This means that the formation of O_2 and H_2O_2 cannot account for the continuing loss of H_2O. A possible explanation could be that the cap on top of the ice may, in fact, enhance the bulk chemistry, as radicals that normally would be photodesorbing would then be forced to remain inside the ice matrix. However, we would expect to see a clear increase of new reaction products, such as H_2O_2, in that case, and this is definitely not what occurs. This observation is also in line with other species studied in earlier work using Ar caps, both for nondissociative (Paardekooper et al. 2016b) and dissociative (Bulak et al. 2020) ice constituents. Along the same line, such radicals may get trapped in the capped ice, thus decreasing the H_2O abundance but not being recognized as originating from water. This, however, should also result in H_2O reformation and is therefore unlikely. For these reasons, we looked into other options. A possible explanation is linked to a morphology change, at least for higher fluences.

The deposition of H_2O molecules at a cold 10–20 K substrate is known to result in the formation of amorphous and consequently low-density ice. It is also known that this "porous" structure starts compacting upon UV irradiation, for example, through a decrease (or full loss) of the dangling-OH bond signals, resulting in a higher density (read thinner ice) and a stronger hydrogen-bonded network. For our experiments, this means that data points taken at the beginning and after 5 hours of UV irradiation monitor ices with different densities and internal binding energies. This also means that upon laser ablation, for the long time irradiation experiments, the actual number of water molecules in the plume may be lower, and this would explain the unaccounted loss of H_2O within a single experiment in the absolute amount. Whether this is really the process at work is not clear. We stress, though, that we do not expect that this ambiguity influences the photodesorption rate we present for typically lower fluence, as this rate was obtained by subtraction of the results of Ar-capped and Ar-uncapped experiments. In this case, the bulk effects impact both experiments equally as strong.

5. Astrophysical implications

The values used in the past in gas-grain models for the photodesorption rate of ASW are very close to the value derived in this work. Our value, which we derived following a different experimental concept, offers a more strict upper limit. A detailed astrochemical model of molecular clouds by Hollenbach et al. (2009) shows that photodissociation and photodesorption

are the dominant physical processes impacting the gas-phase abundances from the edges until intermediate depths into the cloud. In their model, at the onset of the water ice freeze-out, the water vapor abundance is 98%, due to photodesorption of H_2O that has formed on grains, and the remainder (of the gas-phase abundance) forms through low temperature gas-phase chemistry. Deeper into the cloud, the percentage drops to 70%, and at intermediate depths into the cloud, it goes up again to 92%. In this model, the intact (H_2O) and dissociative (OH from H_2O ice) photodesorption rates are set to 1×10^{-3} and 2×10^{-3} per incident UV photon, respectively. The photodesorption of O_2 was considered only from pure O_2 ices at 1×10^{-3} molecule photon^{-1}. These rates were used to reproduce the gas-phase H_2O and (when applicable) O_2 abundances toward molecular cloud B68, a star-forming cloud in Orion, NGC 2024, and ρ Ophiuchus (Hollenbach et al. 2009; Larsson et al. 2007). In a less-detailed model by Schmalzl et al. (2014), the same intact photodesorption rate, combined with photodissociation and freeze-out rates, successfully matches the abundances of water vapor toward the cold regions of pre- and protostellar cores. Additionally, the reactive photodesorption (of O_2) was not taken into account in this study.

Models mentioned above use previous laboratory values for intact photodesorption that are largely in line with our work. However, the values for dissociative desorption rate (OH) seem to be consistently lower (see Table 1) than currently adapted in models. We recommend that these values be adapted, as the OH radical, released from the grains via a nonthermal mechanism, contributes to the formation of simple molecules, such as CO, CO_2, NO, and H_2O, as well as complex organic molecules, such as $HCOOCH_3$ (Charnley et al. 2001; Vasyunin & Herbst 2013; Shannon et al. 2013; Vasyunin et al. 2017). In addition, based on the work presented here, we propose for future work that the reactive photodesorption rate of O_2 be added to the astrochemical models.

In our experiments, the photoconversion depletes the H_2O column density twice as fast as the photodesorption. The formation of photoproducts O_2 and H_2O_2 can account for the initial photoconversion of water until a UV fluence of 9.0×10^{17} photon cm^{-2}, each at a formation level of 1% of H_2O (Bulak et al. 2022). The continuing formation of OH radicals can be of significance for the ice chemistry in mixed ices, opening pathways toward oxygen-carrying molecules such as CO_2, CH_3OH, HCOOH, or $HCOOCH_3$ (Öberg et al. 2009a, 2010; Garrod et al. 2008).

We find it important to note that while water is the dominant component of interstellar ices, other species, including CO_2, CH_4, NH_3, and CH_3OH, are present and expected to impact the photoconversion as well as the photodesorption rates derived for pure water ice. The inclusion of less abundant constituents of interstellar ices in water ice strongly affects the observed photoconversion. These effects are outlined by Öberg et al. (2010), and they demonstrate that the recombination reactions of water are inhibited by up to an order of magnitude due to competitive reactions with other radicals in the ice. In a recent study of photolysis of mixed ices of H_2O:CO_2, an increasing amount of CO_2 in the initial composition resulted in a more efficient photodepletion of water, a shift in the photoproduct yields to carbon-bearing species, and a corresponding decrease in the absolute formation yield of O_2 and H_2O_2 (Bulak et al. 2022). It is also expected that the photodesorption rates of species in mixed ices will differ from its pure equivalents. This will be the topic of future work, as the work presented here is on pure water ice, but the applied

method has the potential to also derive photodesorption rates for different species in mixed ices.

6. Conclusions

A quantification of photodesorption rates and separating this process from the photoconversion of ASW are crucial, as they allow us to balance water abundances between ice and gas in astronomical environments such as dense molecular clouds. In this work, we applied an alternative, independent measuring technique of LDPI TOF MS to determine the photodesorption rate during the UV photolysis of porous amorphous water ice at 20 K. We derived the total photodesorption rate to be $(1.0 \pm 0.2) \times 10^{-3}$ per incident UV photon, which accounts for the sum of intact desorption H_2O, desorption of H_2O photodissociation products (H, OH, or O), and reactive desorption (H_2, O_2). This is well in line with other values, experimentally derived and used in models. This value is an average for the photon energy range equivalent to the secondary UV field in the ISM (7–10.2 eV). Based on this value, we placed an upper limit on the relative contribution of other water depleting channels. Both the intact (H_2O) and dissociative (OH) desorption rates have an upper limit equal to 1.0×10^{-3} per incident UV photon, while for reactive desorption (O_2), the limit is equal to 0.5×10^{-3} per incident UV photon, as one H_2O molecule carries one oxygen atom. We note that these values are derived for pure water ice. Even though water is the dominant species in interstellar ices, other species may also be present, and they can affect these values, mainly because of additional chemical reaction pathways. Future research therefore also needs to focus on photodesorption rates of mixed ices, and with the new technique presented here, this will be possible.

References

Andersson, S., & van Dishoeck, E. F. 2008, A&A, 491, 907
Andersson, S., Al-Halabi, A., Kroes, G.-J., & van Dishoeck, E. F. 2006, J. Chem. Phys., 124, 064715
Arasa, C., Andersson, S., Cuppen, H. M., van Dishoeck, E. F., & Kroes, G. J. 2010, J. Chem. Phys., 132, 184510
Arasa, C., Andersson, S., Cuppen, H. M., van Dishoeck, E. F., & Kroes, G. J. 2011, J. Chem. Phys., 134, 164503
Arasa, C., Koning, J., Kroes, G.-J., Walsh, C., & van Dishoeck, E. F. 2015, A&A, 575, A121
Bergin, E. A., Langer, W. D., & Goldsmith, P. F. 1995, ApJ, 441, 222
Bergin, E. A., Melnick, G. J., Stauffer, J. R., et al. 2000, ApJ, 539, L129
Bertin, M., Romanzin, C., Doronin, M., et al. 2016, ApJ, 817, L12
Boogert, A. C. A., Pontoppidan, K. M., Knez, C., et al. 2008, ApJ, 678, 985
Boogert, A. C. A., Gerakines, P. A., & Whittet, D. C. B. 2015, ARA&A, 53, 541
Boonman, A. M. S., Doty, S. D., van Dishoeck, E. F., et al. 2003, A&A, 406, 937
Bulak, M., Paardekooper, D. M., Fedoseev, G., & Linnartz, H. 2020, A&A, 636, A32
Bulak, M., Paardekooper, D. M., Fedoseev, G., & Linnartz, H. 2021, A&A, 647, A82
Bulak, M., Paardekooper, D. M., Fedoseev, G., et al. 2022, A&A, 657, A120
Caselli, P., Keto, E., Bergin, E. A., et al. 2012, ApJ, 759, L37
Ceccarelli, C., Bacmann, A., Boogert, A., et al. 2010, A&A, 521, L22
Charnley, S. B., Rodgers, S. D., & Ehrenfreund, P. 2001, A&A, 378, 1024
Chen, Y. J., Chuang, K. J., Muñoz Caro, G. M., et al. 2014, ApJ, 781, 15
Crouse, J., Loock, H. P., & Cann, N. M. 2015, J. Chem. Phys., 143, 034502
Cruz-Diaz, G. A., Martín-Doménech, R., Moreno, E., Muñoz Caro, G. M., & Chen, Y.-J. 2018, MNRAS, 474, 3080
DeSimone, A. J., Crowell, V. D., Sherrill, C. D., & Orlando, T. M. 2013, J. Chem. Phys., 139, 164702
Dominik, C., Ceccarelli, C., Hollenbach, D., & Kaufman, M. 2005, ApJ, 635, L85
Fayolle, E. C., Bertin, M., Romanzin, C., et al. 2011, ApJ, 739, L36
Fillion, J.-H., Dupuy, R., Féraud, G., et al. 2022, ACS Earth Space Chem., 6, 100
Flagey, N., Goldsmith, P. F., Lis, D. C., et al. 2013, ApJ, 762, 11
Garrod, R. T., Widicus Weaver, S. L., & Herbst, E. 2008, ApJ, 682, 283
Gerakines, P. A., Schutte, W. A., & Ehrenfreund, P. 1996, A&A, 312, 289
Gibb, E. L., Whittet, D. C. B., Boogert, A. C. A., & Tielens, A. G. G. M. 2004, ApJS, 151, 35
Gredel, R., Lepp, S., Dalgarno, A., & Herbst, E. 1989, ApJ, 347, 289
Harada, N., Herbst, E., & Wakelam, V. 2010, ApJ, 721, 1570
Hartogh, P., Lis, D. C., Bockelée-Morvan, D., et al. 2011, Nature, 478, 218
Hogerheijde, M. R., Bergin, E. A., Brinch, C., et al. 2011, Science, 334, 338
Hollenbach, D., Kaufman, M. J., Bergin, E. A., & Melnick, G. J. 2009, ApJ, 690, 1497
Ioppolo, S., Cuppen, H. M., Romanzin, C., van Dishoeck, E. F., & Linnartz, H. 2008, ApJ, 686, 1474
Ioppolo, S., Cuppen, H. M., Romanzin, C., van Dishoeck, E. F., & Linnartz, H. 2010, Phys. Chem. Chem. Phys. 12, 12065
Jensen, M. J., Bilodeau, R. C., Safvan, C. P., et al. 2000, ApJ, 543, 764
Kim, Y. K., Irikura, K. K., Rudd, M. E., & Ali, M. A. 2014, Electron-Impact Ionization Cross Section for Ionization and Excitation Database (version 3.0)
Kobayashi, K. 1983, J. Phys. Chem., 87, 4317
Koning, J., Kroes, G. J., & Arasa, C. 2013, J. Chem. Phys., 138, 104701
Lamberts, T., Cuppen, H. M., Ioppolo, S., & Linnartz, H. 2013, Phys. Chem. Chem. Phys., 15, 8287
Larsson, B., Liseau, R., Pagani, L., et al. 2007, A&A, 466, 999
Ligterink, N. F. W., Paardekooper, D. M., Chuang, K.-J., et al. 2015, A&A, 584, A56
Martín-Doménech, R., Manzano-Santamaría, J., Muñoz Caro, G. M., et al. 2015, A&A, 584, A14
Miyauchi, N., Hidaka, H., Chigai, T., et al. 2008, Chem. Phys. Lett., 456, 27
Muñoz Caro, G. M., Jiménez-Escobar, A., Martín-Gago, J. Á., et al. 2010, A&A, 522, A108
Nishi, N., Shinohara, H., & Okuyama, T. 1984, J. Chem. Phys., 80, 3898
Öberg, K. I., Garrod, R. T., van Dishoeck, E. F., & Linnartz, H. 2009a, A&A, 504, 891
Öberg, K. I., Linnartz, H., Visser, R., & van Dishoeck, E. F. 2009b, ApJ, 693, 1209
Öberg, K. I., van Dishoeck, E. F., Linnartz, H., & Andersson, S. 2010, ApJ, 718, 832
Oka, A., Inoue, A. K., Nakamoto, T., & Honda, M. 2012, ApJ, 747, 138
Paardekooper, D. M., Bossa, J. B., Isokoski, K., & Linnartz, H. 2014, Rev. of Sci. Instr., 85, 104501
Paardekooper, D. M., Bossa, J. B., & Linnartz, H. 2016a, A&A, 592, A67
Paardekooper, D. M., Fedoseev, G., Riedo, A., & Linnartz, H. 2016b, A&A, 596, A72
Pontoppidan, K. M., van Dishoeck, E. F., & Dartois, E. 2004, A&A, 426, 925
Prasad, S. S., & Tarafdar, S. P. 1983, ApJ, 267, 603
Schmalzl, M., Visser, R., Walsh, C., et al. 2014, A&A, 572, A81
Schnepp, O., & Dressler, K. 1960, J. Chem. Phys., 33, 49
Shannon, R. J., Blitz, M. A., Goddard, A., & Heard, D. E. 2013, Nat. Chem., 5, 745
Snell, R. L., Howe, J. E., Ashby, M. L. N., et al. 2000, ApJ, 539, L101
Tielens, A. G. G. M., & Hagen, W. 1982, A&A, 114, 245
Vasyunin, A. I., & Herbst, E. 2013, ApJ, 769, 34
Vasyunin, A. I., Caselli, P., Dulieu, F., & Jiménez-Serra, I. 2017, ApJ, 842, 33
Walsh, C., Millar, T. J., & Nomura, H. 2010, ApJ, 722, 1607
Westley, M. S., Baragiola, R. A., Johnson, R. E., & Baratta, G. A. 1995, Nature, 373, 405
Whittet, D. C. B., Poteet, C. A., Chiar, J. E., et al. 2013, ApJ, 774, 102
Willacy, K. 2007, ApJ, 660, 441
Willacy, K., & Langer, W. D. 2000, ApJ, 544, 903
Wilson, C. D., Mason, A., Gregersen, E., et al. 2003, A&A, 402, L59